

Interband scattering- and nematicity-induced quantum oscillation frequency in FeSe

Valentin Leeb^{1,2} and Johannes Knolle^{1,2,3}

¹Technical University of Munich, TUM School of Natural Sciences,
Physics Department, TQM, 85748 Garching, Germany

²Munich Center for Quantum Science and Technology (MCQST), Schellingstr. 4, 80799 München, Germany

³Blackett Laboratory, Imperial College London, London SW7 2AZ, United Kingdom

(Dated: September 11, 2023)

Understanding the nematic phase observed in the iron-chalcogenide materials is crucial for describing their superconducting pairing. Experiments on FeSe_{1-x}S_x showed that one of the slow Shubnikov–de Haas quantum oscillation frequencies disappears when tuning the material out of the nematic phase via chemical substitution or pressure, which has been interpreted as a Lifshitz transition [Coldea *et al.*, npj Quant Mater 4, 2 (2019), Reiss *et al.*, Nat. Phys. 16, 89–94 (2020)]. Here, we present a generic, alternative scenario for a nematicity-induced sharp quantum oscillation frequency which disappears in the tetragonal phase and is not connected to an underlying Fermi surface pocket. We show that different microscopic interband scattering mechanisms – for example, orbital-selective scattering – in conjunction with nematic order can give rise to this quantum oscillation frequency beyond the standard Onsager relation. We discuss implications for iron-chalcogenides and the interpretation of quantum oscillations in other correlated materials.

Introduction.– The availability of experimental methods, which are able to correctly identify the low energy electronic structure of quantum materials, is critical for understanding their emergent phenomena like superconductivity, various density waves or nematic orders. For example, angle-resolved photoemission spectroscopy (ARPES) on the cuprate materials confirmed that a single band Hubbard-like description is a reasonable starting point for modelling their low energy structure [1], but iron-based superconductors require a multi-band, multi-orbital description [2–4]. Beyond ARPES, quantum oscillation (QO) measurements are an exceptionally sensitive tool for measuring Fermi surface (FS) geometries as well as interaction effects via extracting the effective masses from the temperature dependence [5]. For example, QO studies famously confirmed the presence of a closed FS pocket in underdoped cuprates in a field [6, 7] or observed the emergence of small pockets in the spin density wave parent phase of iron-based superconducting compounds [8–10].

The interpretation of QOs, as measured in transport or thermodynamic observables, is based on the famous Onsager relation, which ascribes each QO frequency to a semi-classical FS orbit [5, 13]. In the past years, this canonical description has been challenged by the observation of *anomalous* QOs in correlated insulators [14, 15] which motivated a number of works revisiting the basic theory of QOs [16–28]. Very recently, forbidden QO frequencies have been reported in the multi-fold semi-metal CoSi [29], which generalize so-called magneto-intersubband oscillations known in coupled 2D electron gases [30–32] to generic bulk metals [33]. In Ref. [29] it was proposed that QO of the quasiparticle lifetime in systems with multiple allowed FS orbits can lead to new combination frequencies without a corresponding semi-classical FS trajectory.

Here, we propose a new explanation for the QO spectra measured in the iron-chalcogenide superconduc-

tor FeSe_{1-x}S_x which leads to an alternative identification of its low energy electronic structure with direct implications for the superconducting pairing. Iron-chalcogenides are unique among the iron-based superconductors as they show an orthorhombic distortion without stripe magnetism, i.e. pristine FeSe is already in a nematic phase [34–36]. Recently it was reported that one of the observed slow QO frequencies (labeled as λ in the experimental data) vanishes when tuning out of the nematic into the tetragonal phase, via pressure in FeSe_{0.89}S_{0.11} [12] or via isoelectronic substitution in FeSe_{1-x}S_x [11]. Following Onsager’s standard theory it has been interpreted as a Lifshitz transition, i.e. a FS pocket present in the nematic phase which disappears at the nematic quantum critical point [12]. As an alternative scenario, we show here that an additional slow QO frequency without an underlying FS orbit can naturally appear in an electronic nematic phase.

Our scenario requires the following features of iron-chalcogenides [37–41]: (i) The FS consists of several pockets, in particular two electron pockets (labeled here as β_x and β_y) around the Y and X point of the Brillouin zone (BZ), see Fig. 1 panel (b). β_x (β_y) has almost pure d_{xz} (d_{yz}) orbital character with some d_{xy} content. They are related to each other via a C_4 rotation in the tetragonal phase. (ii) When tuning into nematic phase with broken rotational symmetry (reduced to C_2) one of the pockets spontaneously increases in size, whereas the other one shrinks, see panel (a). In the QO spectrum, this is visible by the split up of one formerly degenerate QO frequency into 2 frequencies. (iii) A strong inter-pocket scattering between the β_x and β_y pocket exists [34, 42–44]. It can be caused either by orbital selective impurity scattering over the d_{xy} -channel, low-momentum scattering, collective fluctuations or, most likely, a combination of all. As a result, we will show that a new slow QO frequency, set by the difference of the β_x and β_y frequencies, emerges.

We argue that our theory can not only explain the slow SdH QO frequency observed in iron-chalcogenides, but also discuss that it provides further support for the robustness of s_{\pm} superconducting pairing.

We note that we do not aim towards a full quantitative description of the complicated QO spectrum of FeSe but rather focus on presenting a new theory for the additional slow QO frequency appearing in the nematic phase, thus, concentrating on model descriptions with the minimal ingredients of the electronic structure (e.g. neglecting aspects of three-dimensionality).

The paper is organized as follows: We first introduce a basic two-band model which captures the minimal features of an electronic nematic phase transition. We then show that inter-pocket scattering leads to a new QO frequency in a full lattice calculation of the SdH effect, including the orbital magnetic field via Peierls substitution. Next, we discuss a more microscopic multi-orbital description of iron-chalcogenides and identify different scattering mechanisms leading to strong inter-electron pocket coupling. Again, we confirm the emergence of a slow nematicity-induced frequency in a full lattice calculation. We close with a summary and outlook.

Minimal two-pocket model.— First, we consider a minimal model with two electron pockets and the Hamiltonian

$$H_0 = \sum_{\mathbf{k}} (\epsilon_{x,\mathbf{k}} - \delta\mu) d_{x,\mathbf{k}}^\dagger d_{x,\mathbf{k}} + (\epsilon_{y,\mathbf{k}} + \delta\mu) d_{y,\mathbf{k}}^\dagger d_{y,\mathbf{k}} \quad (1)$$

with the dispersion $\epsilon_{x,\mathbf{k}} = -2t_1 \cos k_x + 2t_2 \cos k_y$ and $\epsilon_{y,\mathbf{k}} = 2t_2 \cos k_x - 2t_1 \cos k_y$. It consists of a β_x -FS pocket around the Y-point and a β_y -Fermi pocket around the X-point, see Fig. 1 (b). For $\delta\mu = 0$ the Hamiltonian is invariant under the C_4 rotation $(k_x, k_y) \rightarrow (k_y, -k_x)$, $(d_x, d_y) \rightarrow (d_y, -d_x)$. Additional density-density interactions $\sum_{\mathbf{r}, \alpha, \beta} d_{\alpha,\mathbf{r}}^\dagger d_{\alpha,\mathbf{r}} d_{\beta,\mathbf{r}}^\dagger d_{\beta,\mathbf{r}}$ can induce a nematic transition with a finite orbital asymmetry $\delta\mu \neq 0$ breaking the C_4 rotation symmetry. Mean-field calculations confirm that $\delta\mu$ becomes non-zero for interactions above a critical threshold [45]. Thus, $\delta\mu$ serves as an order parameter for a nematic phase transition, which is manifest in the band structure by the spontaneous growth/shrinking of the two inequivalent pockets, see Fig. 1 (a). We note that additional FS pockets are present in FeSe and change properties of the nematic phase quantitatively but are not relevant for our purpose.

In practice an external parameter λ tunes the effective interaction strength, e.g. via a change of applied pressure [12] or chemical substitution [11]. Again, the precise relation between $\delta\mu(\lambda)$ and λ depends on microscopic details but we assume in the following the generic form of a second order phase transition $\delta\mu \propto (\lambda_c - \lambda)^\alpha \theta(\lambda_c - \lambda)$ and fix, for simplicity, the exponent to be of the standard mean-field behaviour $\alpha = 1/2$.

Following our recent works [29, 33], we introduce a scattering contribution between the two electron pockets

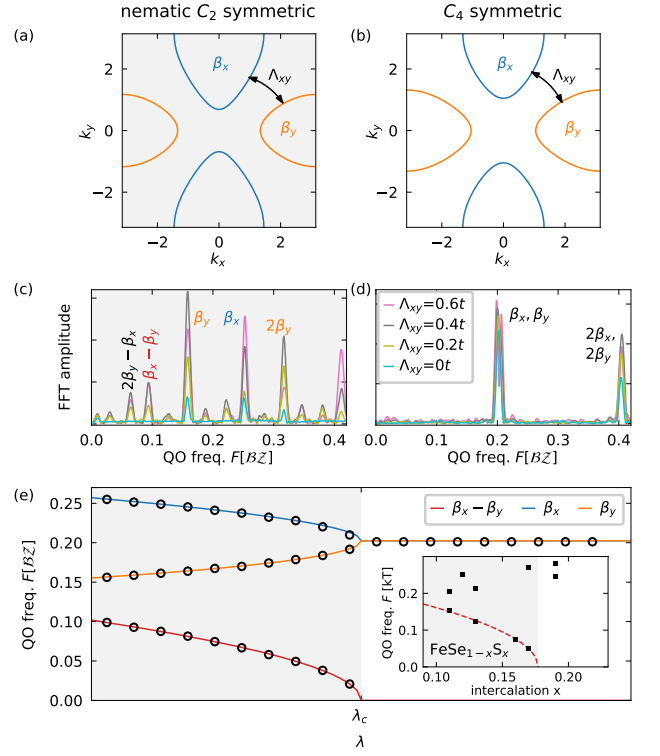


FIG. 1. (b) FS of a minimal model including only 2 electron pockets β_x, β_y with different orbital character. (a) In the nematic phase the β_x pocket spontaneously grows whereas β_y shrinks, see (c) and (d) for representative numerical SdH QO spectra for the different phases. (e) In the nematic phase (gray background) the degenerate frequency of the C_4 symmetric phase splits up into two frequencies (blue, orange), each associated with one FS. When taking interband coupling from impurities (Λ_{xy}), see (a), (b) into account a third frequency (red) which is exactly the difference of the basis frequencies $\beta_x - \beta_y$ appears in the nematic phase. We fixed $t_1/2 = t_2 = t$, $\mu = -3t$. The inset of panel (e) shows the experimentally detected peak frequencies in FeSe $_{1-x}$ S $_x$ [11]. The red dashed line ($\propto \sqrt{\lambda_c - \lambda}$) is a guide to the eye highlighting the emergent frequency in the nematic phase, identified as λ in Ref. [11, 12].

via impurities

$$H_{\text{imp}} = \sum_{\mathbf{r}} \Lambda_{xy,\mathbf{r}} d_{x,\mathbf{r}}^\dagger d_{y,\mathbf{r}} + h.c. \quad (2)$$

where $\Lambda_{xy,\mathbf{r}}$ are drawn randomly, independently and uniformly in space from the interval $[-\Lambda_{xy}/2, \Lambda_{xy}/2]$. On average the system retains its translation and rotation symmetry. For simplicity we set the intraorbital part of the impurities, i.e. Λ_{xx} and Λ_{yy} to zero, as they will only suppress the amplitude of all QO frequencies [33].

We include a magnetic field by standard Peierls substitution, effectively inserting a flux Φ in each plaquette of the square lattice. We have implemented the hopping Hamiltonian with magnetic field and impurities for system sizes up to 300×300 lattice sites. We determined

the conductance through the Landau–Büttiker algorithm using the python package kwant [46] and observed SdH oscillations of the conductance as function of $1/\Phi$. We then analyzed the Fourier transformation in $2\pi/\Phi$ with standard QO techniques, which include subtraction of a polynomial background, zero padding and windowing, see SM. Representative Fourier spectra for the tetragonal (C_4 symmetric) and nematic phase are shown in Fig. 1 (c) and (d), where the frequencies are shown in units of the area of the BZ.

The Fourier spectrum of the SdH oscillations features, as expected from Onsager’s relation, peaks at frequencies $F_\beta = S_\beta/2\pi e$, which correspond to the area of the respective FSs S_β and higher harmonics thereof. As our main finding, the spectrum has clear peaks at combination frequencies in the nematic phase, most dominantly $\beta_x - \beta_y$. Crucially, this frequency does not have an underlying FS or semiclassical orbit of any kind but is a consequence of QO of the quasi-particle lifetime. We note that this is in accordance with our recent analytical work [33], which we confirm here for the first time in a numerical lattice calculation.

In Fig. 1 (e), we plot the frequencies of the 3 strongest signals for weak inter-orbit scattering as a function of the external parameter λ tuning through the nematic transition. When increasing the nematic order, the main frequency peak splits into two, and the additional low-frequency $\beta_x - \beta_y$ oscillation emerges similar to the experimental data, see inset.

Multi-orbital model.– After studying a minimal two-band model, we next want to understand the possible origin of a strong inter-pocket scattering. Therefore, we need to take the multi-orbital character of iron-chalcogenides into account. In order to keep the numerical lattice calculations tractable we focus on the following key features, see Fig. 2 (a): (i) Two electron-like elliptical pockets β_x and β_y around the Y and X points which have mainly d_{xz} and d_{yz} orbital character but in addition also an admixture of d_{xy} orbitals; (ii) One (or depending on the precise model and parameter regime also two) hole-like circular pockets γ around the Γ point which have mixed d_{xz} and d_{yz} orbital character; (iii) Only the electron pockets β_x and β_y have additional d_{xy} orbital character.

All features (i)-(iii) are captured by a three orbital model [45] with d_{xz} , d_{yz} , and d_{xy} orbitals (denoted by xz, yz, xy). Introducing $\Psi_{\mathbf{k}} = (d_{\mathbf{k},xz}, d_{\mathbf{k},yz}, d_{\mathbf{k},xy})$, the Hamiltonian reads

$$H_0 = \sum_{\mathbf{k}} \Psi_{\mathbf{k}}^\dagger (T(\mathbf{k}) - \mu) \Psi_{\mathbf{k}} + \delta\mu \begin{pmatrix} d_{\mathbf{k},xz} \\ d_{\mathbf{k},yz} \end{pmatrix}^\dagger \sigma^z \begin{pmatrix} d_{\mathbf{k},xz} \\ d_{\mathbf{k},yz} \end{pmatrix} \quad (3)$$

where $T(\mathbf{k})$ is a 3×3 matrix which depends on the electronic hopping strengths between the orbitals. The real-space form of the Hamiltonian, $T(\mathbf{k})$ and the parameters are given in the SM.

In the tetragonal phase, with $\delta\mu = 0$, the Hamiltonian is again invariant under the C_4 rotation $(k_x, k_y) \rightarrow$

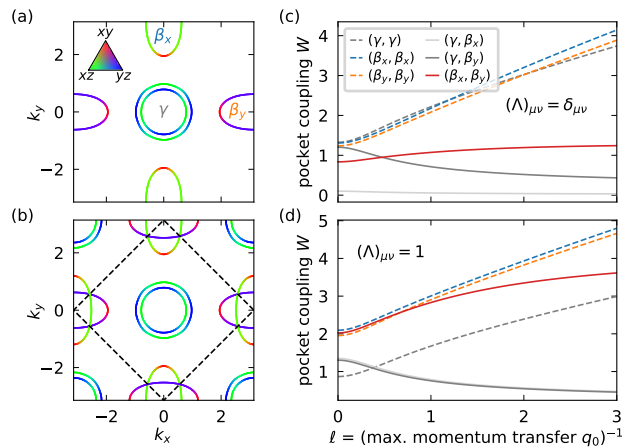


FIG. 2. Panel (a): Typical FS of the three-orbital model in the nematic phase. Colors indicate the orbital character. Panel (b): Buckling enlarges the unit cell which leads to a backfolded FS in the reduced Brillouin zone (black dashed). Panel (c): FS integrated inter- and intrapocket scattering strength for $(\Lambda)_{\mu\nu} = \delta_{\mu\nu}$ showing that the coupling W_{β_x, β_y} is dominant. It increases for small momentum scattering, i.e. $1/q_0 \rightarrow \infty$. Any other type of interorbit scattering enlarges the coupling of β_x and β_y even further, see panel (d) where $(\Lambda)_{\mu\nu} = 1$.

$(k_y, -k_x), (d_x, d_y) \rightarrow (d_y, -d_x)$. Similar to the toy model from above, a nematic phase is characterized by a finite $\delta\mu$ where the rotation symmetry is reduced to a \mathbb{Z}_2 reflection symmetry / C_2 rotation symmetry.

The parameter $\delta\mu$ is again an effective, emergent parameter but now we can relate its microscopic origin to orbital ordering. For example the interorbital density interaction between xz and yz orbitals

$$H_{\text{int}} = U \sum_{\mathbf{r}} d_{\mathbf{r},xz}^\dagger d_{\mathbf{r},xz} d_{\mathbf{r},yz}^\dagger d_{\mathbf{r},yz}. \quad (4)$$

can be decoupled in mean-field to obtain a self-consistent order parameter for the nematic (now orbital ordering) transition leading to $\delta\mu = U (\langle d_{\mathbf{r},xz}^\dagger d_{\mathbf{r},xz} \rangle - \langle d_{\mathbf{r},yz}^\dagger d_{\mathbf{r},yz} \rangle) / 2$. A typical FS within the nematic phase is shown in Fig. 2 (a).

We note that this role of orbital ordering, or an imbalance of the orbital occupation, in the nematic phase has been confirmed in a number of experiments [38, 39] most recently via X-ray linear dichroism [40]. While our minimal three-orbital model captures the key features, the precise asymmetry of the γ hole pocket(s) in the nematic phase of FeSe is more complicated however its shape does not affect our new findings.

Impurities and orbital selective scattering.– As confirmed in our two-band model numerically and expected from analytical calculations [33], a nematicity induced difference frequency requires a sizeable coupling of the pockets β_x and β_y . The absence of other frequency combinations points towards a negligible coupling of β_i and

γ . We next investigate the origin of this coupling in terms of the d -orbital dependent scattering. Therefore, we consider impurities in the orbital basis

$$H_{\text{imp}} = \sum_{\mathbf{r}} \sum_{\mathbf{r}_i} V(\mathbf{r} - \mathbf{r}_i) \Psi_{\mathbf{r}}^\dagger \Lambda_{\mathbf{r}_i} \Psi_{\mathbf{r}} \quad (5)$$

with the scattering vertex $\Lambda_{\mathbf{r}_i}$ a random hermitian matrix with mean 0 and variance Λ^2 . Note, impurities respect the $\pi/2$ -rotation symmetry only on average. Similarly, impurities located at \mathbf{r}_i are distributed randomly and uniformly such that the systems remains on average translationally invariant. We model the interaction of electrons with impurities by a screened Coulomb interaction V_ℓ of Yukawa type with screening length ℓ [47].

We quantify the coupling $W_{\alpha,\alpha'}$ of FS orbits α and α' by integrating the scattering amplitudes of all possible processes between them

$$W_{\alpha,\alpha'} = \oint_{\mathbf{k} \in \alpha} \oint_{\mathbf{k}' \in \alpha'} \left| \begin{array}{c} \star \\ \mathbf{k}' - \mathbf{k} \\ \mathbf{k} \quad \mathbf{k}' \end{array} \right| \quad (6)$$

$$= \oint_{\mathbf{k} \in \alpha} \oint_{\mathbf{k}' \in \alpha'} |\tilde{V}_\ell(\mathbf{k}' - \mathbf{k}) \mathcal{U}(\mathbf{k}')^\dagger \Lambda \mathcal{U}(\mathbf{k})|. \quad (7)$$

Here, $\mathcal{U}(\mathbf{k})$ is the transformation which diagonalizes H_0 for a each momentum. The Fourier transform of the screened Coulomb interaction $\tilde{V}_\ell = \mathcal{N}_\ell / (\mathbf{k}^2 + 1/\ell^2)$ allows only scattering up to a maximal momentum $q_0 = 1/\ell$ (\mathcal{N}_ℓ is a normalization constant).

Iron-chalcogenides have a 2 site unit cell [37], which leads to a folding of the $T(\mathbf{k} + (\pi, \pi))$ bands onto the $T(\mathbf{k})$ bands. The FS in the reduced Brillouin zone is shown in Fig. 2 (b), where now the pockets β_x and β_y lay on top of each other. This admits a large scattering between the β_x and β_y pockets because the screened Coulomb interaction favors low-momentum scattering. In Fig. 2 (c) and (d) we show quantitatively that for diagonal or uniform scattering vertices Λ in the orbital components, the coupling W_{β_x,β_y} is the biggest inter-pocket coupling for a sizeable screening length $\ell \gtrsim 0.5$ and of the same size as the intra-orbit couplings.

There are several additional mechanisms which increase W_{β_x,β_y} even further. Crucially, orbital-selective scattering, i.e. a dominating $\Lambda_{xy,xy}$ component of the vertex, leads to a large coupling of exclusively β_x and β_y pockets. Additionally, any off-diagonal element of Λ , i.e. xz/yz to xy and xz to yz scattering, strongly enhances the inter-pocket coupling W_{β_x,β_y} . Overall, there is generically a sizeable coupling between the electron pockets.

An exclusive coupling of the electron pockets β_x, β_y can be modelled by orbital selective scattering over the $\Lambda_{xy,xy}$ channel. The analysis above suggests that this coupling is indeed dominating. For our numerical simulation of the SdH effect we, therefore, focus on short-ranged impurities $V(\mathbf{r}) \propto \delta(\mathbf{r})$ with an orbital selective scattering vertex $(\Lambda)_{ij} = \delta_{i3}\delta_{j3}\Lambda_{xy}$ with only the xy component $\Lambda_{xy,xy}$ being non-zero. We note that experiments indeed suggest

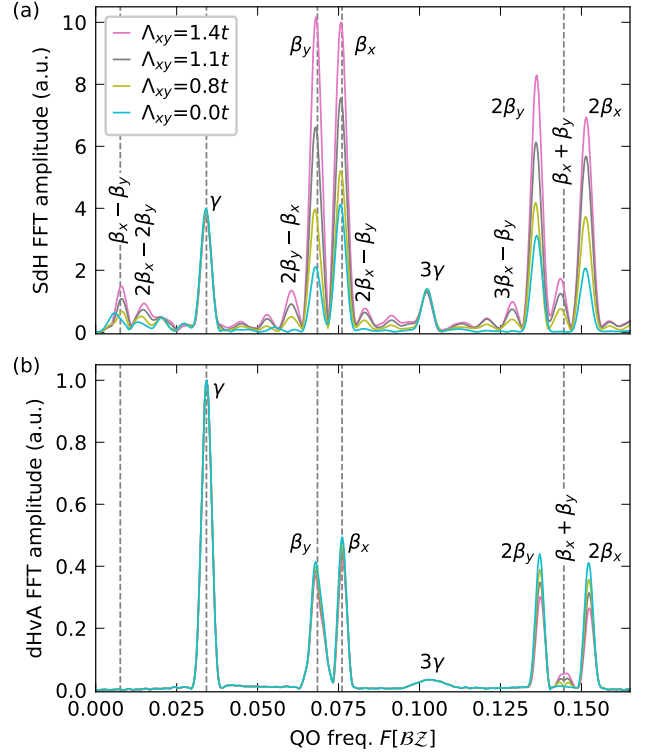


FIG. 3. Numerically computed QO spectra for the parameters regime generating the FSs shown in Fig. 2 (a). In (a) we analyzed the conductance whereas in (b) we analyzed the density of states $\rho(\mu)$. The theoretical prediction for the three basis frequencies and the sum- and difference frequency, based on the area of the FSs, are indicated as grey dashed lines.

that the xy -orbital part of the FS is heavy, leading to a large dominating density of d_{xy} -states for scattering [37].

Slow QO frequency from orbital selective scattering.— Finally, we evaluate the conductance in orbital magnetic fields through samples of sizes up to 400×400 sites with orbital selective impurities within the nematic phase. The dominant SdH peaks in the Fourier spectrum, see Fig. 3 panel (a), are set by the FSs β_x, β_y, γ and higher harmonics thereof. The combination frequencies $\beta_x - \beta_y$ and $\beta_x + \beta_y$ are clearly visible and, additionally, a variety of subleading higher order terms appear whose strength depends on the strength of the impurity scattering. In the lower panel (b) we show the spectrum of the density of states, which corresponds to QO of thermodynamic observables like the de Haas-van Alphen (dHvA) effect. In contrast to the SdH effect, the slow difference frequency is absent in the dHvA effect. The reason is that the latter only depends on the scattering via the Dingle factor whereas scattering dominates transport [29, 33], which is also confirmed by the strong (weak) dependence of the QO signals for the upper (lower) panels. Thus, a careful comparison between QO frequencies of SdH and dHvA can confirm our unusual QO without a FS orbit.

Discussion and Conclusion.— We have shown that a

robust slow QO frequency emerges in minimal models of iron-chalcogenides. The key ingredients were the broken rotational symmetry between the electron pockets in the nematic phase and an efficient coupling between these pockets. The latter can originate from an orbital selective scattering, e.g. a dominating impurity contribution of the d_{xy} orbital. We provided full numerical lattice calculations with orbital magnetic fields, which also confirm recent analytical works on difference frequency QOs without semiclassical orbits beyond the Onsager relation [29, 33]. Further supporting evidence of our scenario is that the experimentally extracted masses from the temperature dependence of the QOs [11] is in accordance with our analytical predictions [33], namely the mass of the slow frequency roughly equals the difference of the ones of the electron pockets.

Of course, neither our effective two-band nor the three-orbital model (which is already challenging numerically) captures all details of the complicated electronic structure of iron-chalcogenides [37]. In fact, we have neglected any correlation effects, which could further increase scattering between the electron pockets, e.g. by collective spin fluctuations. However, our scenario requires no preconditions except a finite coupling of the electron pockets via scattering. Therefore, we expect our scenario to be reproducible in any microscopic model of iron-chalcogenides. In summary, we argue that our results are a robust feature of the nematic phase of iron-chalcogenides and elucidate that no additional pocket of a nematic Lifshitz transition is required to explain the QO experiments [11, 12].

The correct assignment of QO frequencies with putative FS orbits is crucial for correctly identifying the electronic structure in iron-chalcogenides and beyond. Alas, our scenario of sharp QOs without FS orbits further complicates the interpretation of QO data. However, it also provides novel insights into subtle details of quasiparticle scattering otherwise inaccessible in experiments.

We showed that the slow QO frequency of iron-chalcogenides can be explained by the presence of orbital selective impurity scattering, which has implications for the SC pairing symmetry. It is normally expected that impurities, as necessarily present in heavily disordered $\text{FeSe}_{1-x}\text{S}_x$ [48], suppress s^\pm superconductivity [49, 50]. However, the orbital selective scattering does *not* couple the electron and hole pockets, which would be detrimental for s^\pm pairing. Thus, the new QO mechanism possibly explains the robustness of superconductivity in the iron-chalcogenides.

We hope that the observation and quantification of similar QO frequencies can lead to a more precise identification of the electronic structure of other correlated electron materials.

Data and code availability.— Code and data related to this paper are available on Zenodo [51] from the authors upon reasonable request.

ACKNOWLEDGMENTS

We acknowledge helpful discussion and related collaborations with N. Huber, M. Wilde and C. Pfeiderer. We thank A. Chubukov, A. Coldea and T. Shibauchi, for helpful discussions and comments on the manuscript. V. L. acknowledges support from the Studienstiftung des deutschen Volkes. J. K. acknowledges support from the Imperial-TUM flagship partnership. The research is part of the Munich Quantum Valley, which is supported by the Bavarian state government with funds from the Hightech Agenda Bayern Plus.

\mathcal{M}	t_1	t_2	t_3	t_4	t_5	t_6	t_7	t_8	Δ_{xy}	μ	h_y
\mathcal{C}	0.2t	0.6t	0.3t	-0.1t	2t	3t	-2t	t	4t	2.7t	0

TABLE I. The tight-binding parameters used throughout this manuscript.

Appendix A: 3-orbital tight-binding model

The Hamiltonian features nearest- and next-nearest-neighbor hoppings:

$$\begin{aligned}
H_0 = & \sum_{\mathbf{r}} \Psi_{\mathbf{r}+\hat{x}}^\dagger \begin{pmatrix} t_2 & 0 & t_7 \\ 0 & t_1 & 0 \\ -t_7 & 0 & t_5 \end{pmatrix} \Psi_{\mathbf{r}} + \Psi_{\mathbf{r}+\hat{y}}^\dagger \begin{pmatrix} t_1 & 0 & 0 \\ 0 & t_2 & t_7 \\ 0 & -t_7 & t_5 \end{pmatrix} \Psi_{\mathbf{r}} + \Psi_{\mathbf{r}+\hat{x}+\hat{y}}^\dagger \begin{pmatrix} t_3 & -t_4 & t_8 \\ -t_4 & t_3 & t_8 \\ -t_8 & -t_8 & t_6 \end{pmatrix} \Psi_{\mathbf{r}} \\
& + \Psi_{\mathbf{r}+\hat{x}-\hat{y}}^\dagger \begin{pmatrix} t_3 & t_4 & t_8 \\ t_4 & t_3 & -t_8 \\ -t_8 & t_8 & t_6 \end{pmatrix} \Psi_{\mathbf{r}} + \text{h.c.} + \Psi_{\mathbf{r}}^\dagger \begin{pmatrix} -\mu - \delta\mu & -ih_y & 0 \\ ih_y & -\mu + \delta\mu & 0 \\ 0 & 0 & \Delta_{xy} - \mu \end{pmatrix} \Psi_{\mathbf{r}}
\end{aligned} \tag{A1}$$

Defining $\Psi_{\mathbf{r}} = \frac{1}{\sqrt{N}} \sum_{\mathbf{k}} e^{-i\mathbf{k}\mathbf{r}} \Psi_{\mathbf{k}}$ we obtain

$$H_0 = \sum_{\mathbf{k}} \Psi_{\mathbf{k}}^\dagger (T(\mathbf{k}) - \mu) \Psi_{\mathbf{k}} + \delta\mu \begin{pmatrix} d_{\mathbf{k},xz} \\ d_{\mathbf{k},yz} \end{pmatrix}^\dagger \sigma^z \begin{pmatrix} d_{\mathbf{k},xz} \\ d_{\mathbf{k},yz} \end{pmatrix} \tag{A2}$$

where

$$T_{11}(k) = 2t_2 \cos k_x + 2t_1 \cos k_y + 4t_3 \cos k_x \cos k_y \tag{A3}$$

$$T_{22}(k) = 2t_1 \cos k_x + 2t_2 \cos k_y + 4t_3 \cos k_x \cos k_y \tag{A4}$$

$$T_{33}(k) = 2t_5 (\cos k_x + \cos k_y) + 4t_6 \cos k_x \cos k_y + \Delta_{xy} \tag{A5}$$

$$T_{12}(k) = T_{21}(k)^* = 4t_4 \sin k_x \sin k_y + ih_y \tag{A6}$$

$$T_{13}(k) = T_{31}(k)^* = 2it_7 \sin k_x + 4it_8 \sin k_x \cos k_y \tag{A7}$$

$$T_{23}(k) = T_{32}(k)^* = 2it_7 \sin k_y + 4it_8 \cos k_x \sin k_y. \tag{A8}$$

The values of the hopping parameters are shown in Tab. I.

Appendix B: Numerical implementation and QO analysis

We have implemented the tight-binding models and calculated the conductance and the density of states for finite magnetic fields using the python package kwant [46]. The main methodological steps are shown in Fig. 4.

We compute the conductance G with a 2-point measurement, see Fig. 4 (a) via the built-in Landau-Büttiker algorithm, which is based on an S-matrix approach. For the 2-orbital model, we used a system size of 300×300 lattice sites and for the 3-orbital model a system size of 400×400 lattice sites.

In this work, we fit the $N_{\text{data}}(I_\Phi)$ data points inside an interval $2\pi/\Phi \in I_\Phi$ with a 4th order polynomial. After subtracting the polynomial we scale the signal with a window and pad it symmetrically with $4N_{\text{data}}(I_\Phi)$ zeros. Then the signal is Fourier transformed and we always show the absolute of the Fourier transformed signal. For Fig. 1 (c) and (d) we used $I_\Phi = [20, 250]$ and a Hamming window. For Fig. 1 (e) we used $I_\Phi = [40, 300]$ and a Hamming window. For Fig. 1 (e) we used $I_\Phi = [40, 300]$ and a Hamming window. For Fig. 3 (a) we used $I_\Phi = [30, 720]$ and a Blackman-Harris window.

We compute the density of states ρ with the kernel polynomial method [52]. For sampling the spectral density, we use 30 randomly chosen vectors such that only the bulk of the system is sampled. Cutting off the edges suppresses edge state effects over bulk effects, simulating the thermodynamic limit. We define the bulk by the set of all lattice points at least 50 sites away from the edges. We used 7000 Chebyshev moments. In Fig. 3 (b) we analyzed $\rho(\omega = 0, \Phi)$ inside the interval $I_\Phi = [90, 720]$ using a Hamming window.

Note for experimental comparison that $B = \frac{\Phi}{2\pi} \frac{\hbar}{ea^2} = \frac{\Phi}{2\pi} \times 4.63\text{kT}$ for a lattice constant $a = 3.77\text{\AA}$ of iron selenides [53]. We work in units where $e = \hbar = a = 1$. Hence, the analyzed I_Φ intervals translate to roughly 6 - 46T.

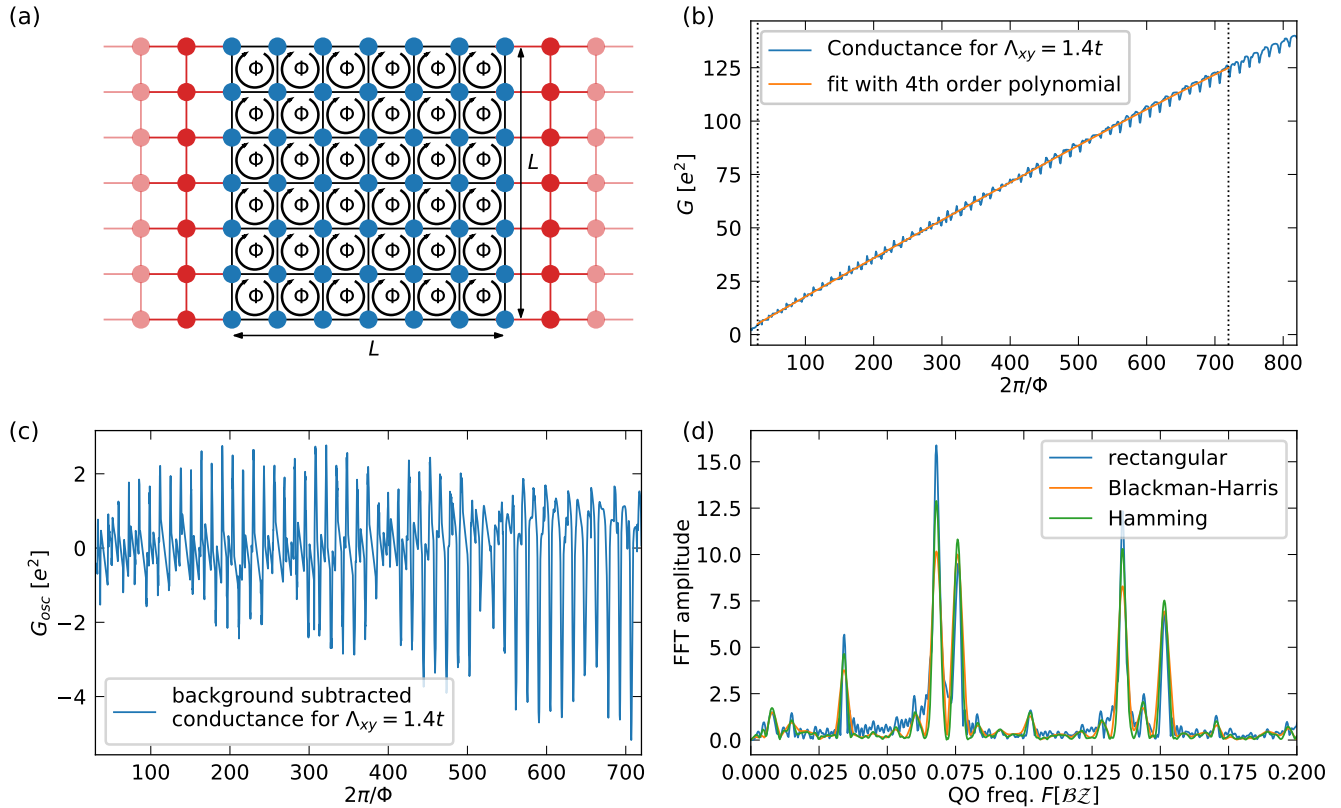


FIG. 4. Panel (a) shows a schematic sketch of the implemented model for conductance simulations. The scattering region (blue vertices) of system size $L \times L$ implements the tight binding model with impurities and each hopping is scaled with a Peierls phase such that flux per plaquette is Φ . The leads (red vertices) are translational invariant, hence are not exposed to the magnetic field and do not have impurities. The conductance G from the left lead to the right lead is computed. Panel (b) shows the exemplary result for the conductance G of the 3-orbital model, i.e. the data shown in Fig. 3. We fit the conductance in the field region I_Φ (marked by the black dotted lines) with a 4th-order polynomial which is then subtracted from the numerical data to obtain the oscillating part of the signal, see panel (c). To obtain a spectrum, panel (d), the oscillating signal is zero padded, scaled with a window and then Fourier transformed. The identified peaks are consistent for different types of chosen windows.

-
- [1] A. Damascelli, Z. Hussain, and Z.-X. Shen, Angle-resolved photoemission studies of the cuprate superconductors, *Reviews of modern physics* **75**, 473 (2003).
- [2] D. Lu, M. Yi, S.-K. Mo, A. Erickson, J. Analytis, J.-H. Chu, D. Singh, Z. Hussain, T. Geballe, I. Fisher, *et al.*, Electronic structure of the iron-based superconductor laofep, *Nature* **455**, 81 (2008).
- [3] P. Richard, T. Qian, and H. Ding, Arpes measurements of the superconducting gap of fe-based superconductors and their implications to the pairing mechanism, *Journal of Physics: Condensed Matter* **27**, 293203 (2015).
- [4] M. Yi, Y. Zhang, Z.-X. Shen, and D. Lu, Role of the orbital degree of freedom in iron-based superconductors, *npj Quantum Materials* **2**, 57 (2017).
- [5] D. Shoenberg, *Magnetic Oscillations in Metals* (Cambridge University Press, 1984).
- [6] N. Doiron-Leyraud, C. Proust, D. LeBoeuf, J. Levallois, J.-B. Bonnemaïson, R. Liang, D. Bonn, W. Hardy, and L. Taillefer, Quantum oscillations and the fermi surface in an underdoped high- t c superconductor, *Nature* **447**, 565 (2007).
- [7] S. E. Sebastian, N. Harrison, and G. G. Lonzarich, Towards resolution of the fermi surface in underdoped high- t c superconductors, *Reports on Progress in Physics* **75**, 102501 (2012).
- [8] S. E. Sebastian, J. Gillett, N. Harrison, P. Lau, D. J. Singh, C. Mielke, and G. Lonzarich, Quantum oscillations in the parent magnetic phase of an iron arsenide high temperature superconductor, *Journal of Physics: Condensed Matter* **20**, 422203 (2008).
- [9] T. Terashima, N. Kurita, M. Tomita, K. Kihou, C.-H. Lee, Y. Tomioka, T. Ito, A. Iyo, H. Eisaki, T. Liang, *et al.*, Complete fermi surface in bafe 2 as 2 observed via shubnikov-de haas oscillation measurements on detwinned single crystals, *Physical Review Letters* **107**, 176402 (2011).
- [10] A. I. Coldea, D. Braithwaite, and A. Carrington, Iron-based superconductors in high magnetic fields, *Comptes*

- Rendus Physique **14**, 94 (2013).
- [11] A. I. Coldea, S. F. Blake, S. Kasahara, A. A. Haghighirad, M. D. Watson, W. Knafo, E. S. Choi, A. McCollam, P. Reiss, T. Yamashita, M. Bruma, S. C. Speller, Y. Matsuda, T. Wolf, T. Shibauchi, and A. J. Schofield, Evolution of the low-temperature fermi surface of superconducting $\text{FeSe}_{1-x}\text{S}_x$ across a nematic phase transition, npj Quantum Materials **4**, 2 (2019).
- [12] P. Reiss, D. Graf, A. A. Haghighirad, W. Knafo, L. Drigo, M. Bristow, A. J. Schofield, and A. I. Coldea, Quenched nematic criticality and two superconducting domes in an iron-based superconductor, Nature Physics **16**, 89 (2020).
- [13] L. Onsager, Interpretation of the de haas-van alphen effect, The London, Edinburgh, and Dublin Philosophical Magazine and Journal of Science **43**, 1006 (1952).
- [14] B. Tan, Y.-T. Hsu, B. Zeng, M. C. Hatnean, N. Harrison, Z. Zhu, M. Hartstein, M. Kiourlappou, A. Srivastava, M. Johannes, *et al.*, Unconventional fermi surface in an insulating state, Science **349**, 287 (2015).
- [15] P. Czajka, T. Gao, M. Hirschberger, P. Lampen-Kelley, A. Banerjee, J. Yan, D. G. Mandrus, S. E. Nagler, and N. Ong, Oscillations of the thermal conductivity in the spin-liquid state of $\alpha\text{-RuCl}_3$, Nature Physics **17**, 915 (2021).
- [16] J. Knolle and N. R. Cooper, Quantum oscillations without a fermi surface and the anomalous de haas-van alphen effect, Physical review letters **115**, 146401 (2015).
- [17] L. Zhang, X.-Y. Song, and F. Wang, Quantum oscillation in narrow-gap topological insulators, Physical review letters **116**, 046404 (2016).
- [18] J. Knolle and N. R. Cooper, Excitons in topological kondo insulators: theory of thermodynamic and transport anomalies in SmB_6 , Physical review letters **118**, 096604 (2017).
- [19] I. Sodemann, D. Chowdhury, and T. Senthil, Quantum oscillations in insulators with neutral fermi surfaces, Physical Review B **97**, 045152 (2018).
- [20] O. Erten, P. Ghaemi, and P. Coleman, Kondo breakdown and quantum oscillations in SmB_6 , Physical review letters **116**, 046403 (2016).
- [21] D. Chowdhury, Y. Werman, E. Berg, and T. Senthil, Translationally invariant non-fermi-liquid metals with critical fermi surfaces: Solvable models, Phys. Rev. X **8**, 031024 (2018).
- [22] H. Shen and L. Fu, Quantum oscillation from in-gap states and a non-hermitian landau level problem, Physical review letters **121**, 026403 (2018).
- [23] P. Lee, Quantum oscillations in the activated conductivity in excitonic insulators: Possible application to monolayer WTe_2 , Physical Review B **103**, L041101 (2021).
- [24] V. Leeb, K. Polyudov, S. Mashhadi, S. Biswas, R. Valentí, M. Burghard, and J. Knolle, Anomalous quantum oscillations in a heterostructure of graphene on a proximate quantum spin liquid, Physical Review Letters **126**, 097201 (2021).
- [25] A. A. Allocca and N. R. Cooper, Low-frequency quantum oscillations from interactions in layered metals, Phys. Rev. Research **3**, L042009 (2021).
- [26] A. A. Allocca and N. R. Cooper, Quantum oscillations in interaction-driven insulators, SciPost Phys. **12**, 123 (2022).
- [27] A. A. Allocca and N. R. Cooper, Fluctuation-dominated quantum oscillations in excitonic insulators (2023), arXiv:2302.06633 [cond-mat.mes-hall].
- [28] V. Leeb and J. Knolle, Quantum oscillations in a doped mott insulator beyond onsager's relation, Phys. Rev. B **108**, 085106 (2023).
- [29] N. Huber, V. Leeb, A. Bauer, G. Benka, J. Knolle, C. Pfleiderer, and M. A. Wilde, Quantum oscillations of the quasiparticle lifetime in a metal, Nature [10.1038/s41586-023-06330-y](https://doi.org/10.1038/s41586-023-06330-y) (2023).
- [30] V. Polyanovsky, Magnetointersubband oscillations of conductivity in a two-dimensional electronic system, Fiz. Tekh. Poluprovodn. **22**, 1408 (1988).
- [31] M. E. Raikh and T. V. Shahbazyan, Magnetointersubband oscillations of conductivity in a two-dimensional electronic system, Phys. Rev. B **49**, 5531 (1994).
- [32] N. S. Averkiev, L. E. Golub, S. A. Tarasenko, and M. Willander, Theory of magneto-oscillation effects in quasi-two-dimensional semiconductor structures, Journal of Physics: Condensed Matter **13**, 2517 (2001).
- [33] V. Leeb and J. Knolle, Theory of difference-frequency quantum oscillations, Phys. Rev. B **108**, 054202 (2023).
- [34] M. D. Watson, T. Yamashita, S. Kasahara, W. Knafo, M. Nardone, J. Béard, F. Hardy, A. McCollam, A. Narayanan, S. Blake, *et al.*, Dichotomy between the hole and electron behavior in multiband superconductor fese probed by ultrahigh magnetic fields, Physical review letters **115**, 027006 (2015).
- [35] S. Kasahara, T. Watashige, T. Hanaguri, Y. Kohsaka, T. Yamashita, Y. Shimoyama, Y. Mizukami, R. Endo, H. Ikeda, K. Aoyama, *et al.*, Field-induced superconducting phase of fese in the BCS-BEC cross-over, Proceedings of the National Academy of Sciences **111**, 16309 (2014).
- [36] T. Terashima, N. Kikugawa, A. Kiswandhi, E.-S. Choi, J. S. Brooks, S. Kasahara, T. Watashige, H. Ikeda, T. Shibauchi, Y. Matsuda, T. Wolf, A. E. Böhrer, F. Hardy, C. Meingast, H. v. Löhneysen, M.-T. Suzuki, R. Arita, and S. Uji, Anomalous fermi surface in fese seen by shubnikov-de haas oscillation measurements, Phys. Rev. B **90**, 144517 (2014).
- [37] A. I. Coldea and M. D. Watson, The key ingredients of the electronic structure of fese, Annual Review of Condensed Matter Physics **9**, 125 (2018).
- [38] S.-H. Baek, D. Efremov, J. Ok, J. Kim, J. Van Den Brink, and B. Büchner, Orbital-driven nematicity in fese, Nature materials **14**, 210 (2015).
- [39] T. Shimojima, Y. Suzuki, T. Sonobe, A. Nakamura, M. Sakano, J. Omachi, K. Yoshioka, M. Kuwata-Gonokami, K. Ono, H. Kumigashira, *et al.*, Lifting of xz/yz orbital degeneracy at the structural transition in detwinned fese, Physical Review B **90**, 121111(R) (2014).
- [40] C. A. Occhialini, J. J. Sanchez, Q. Song, G. Fabbri, Y. Choi, J.-W. Kim, P. J. Ryan, and R. Comin, Spontaneous orbital polarization in the nematic phase of fese, Nature Materials, **1** (2023).
- [41] A. I. Coldea, Electronic nematic states tuned by iso-electronic substitution in bulk $\text{FeSe}_{1-x}\text{S}_x$, Frontiers in Physics **8**, 10.3389/fphy.2020.594500 (2021).
- [42] L. Ortenzi, E. Cappelluti, L. Benfatto, and L. Pietronero, Fermi-surface shrinking and interband coupling in iron-based pnictides, Physical review letters **103**, 046404 (2009).
- [43] M. Breitzkreiz, P. Brydon, and C. Timm, Transport anomalies due to anisotropic interband scattering, Physical Review B **88**, 085103 (2013).
- [44] A. Koshchev, Magnetotransport of multiple-band nearly antiferromagnetic metals due to hot-spot scattering,

- Physical Review B **94**, 125154 (2016).
- [45] M. Daghofer, A. Nicholson, A. Moreo, and E. Dagotto, Three orbital model for the iron-based superconductors, Phys. Rev. B **81**, 014511 (2010).
- [46] C. W. Groth, M. Wimmer, A. R. Akhmerov, and X. Waintal, Kwant: a software package for quantum transport, New Journal of Physics **16**, 063065 (2014).
- [47] H. Bruus and K. Flensberg, *Many-Body Quantum Theory in Condensed Matter Physics: An Introduction*, Oxford Graduate Texts (OUP Oxford, 2004).
- [48] S. Teknowijoyo, K. Cho, M. A. Tanatar, J. Gonzales, A. E. Böhmer, O. Cavani, V. Mishra, P. Hirschfeld, S. Bud'ko, P. Canfield, *et al.*, Enhancement of superconducting transition temperature by pointlike disorder and anisotropic energy gap in fese single crystals, Physical Review B **94**, 064521 (2016).
- [49] D. Efremov, M. Korshunov, O. Dolgov, A. A. Golubov, and P. J. Hirschfeld, Disorder-induced transition between s_{\pm} and s_{++} states in two-band superconductors, Physical Review B **84**, 180512(R) (2011).
- [50] A. Chubukov, Pairing mechanism in fe-based superconductors, Annu. Rev. Condens. Matter Phys. **3**, 57 (2012).
- [51] V. Leeb and J. Knolle, Interband scattering- and nematicity-induced quantum oscillation frequency in fese (2023).
- [52] A. Weiße, G. Wellein, A. Alvermann, and H. Fehske, The kernel polynomial method, Rev. Mod. Phys. **78**, 275 (2006).
- [53] S. Margadonna, Y. Takabayashi, M. T. McDonald, K. Kasperkiewicz, Y. Mizuguchi, Y. Takano, A. N. Fitch, E. Suard, and K. Prassides, Crystal structure of the new FeSe_{1-x} superconductor, Chem. Commun. , 5607 (2008).